

Development of a Perfectly Matched Layer Technique for a Discontinuous–Galerkin Spectral–Element Method

Anirban Garai*, Scott M. Murman[†], and Nateri K. Madavan[‡]

NASA Ames Research Center, Moffett Field, CA, USA

I. Introduction

The numerical simulation of many aerodynamic non-periodic flows of practical interest involves discretized computational domains that often must be artificially truncated. Appropriate boundary conditions are required at these truncated domain boundaries, and ideally, these boundary conditions should be perfectly “absorbing” or “nonreflecting” so that they do not contaminate the flow field in the interior of the domain. The proper specification of these boundaries is critical to the stability, accuracy, convergence, and quality of the numerical solution,¹ and has been the topic of considerable research. The need for accurate boundary specification has been underscored in recent years with efforts to apply higher-fidelity methods (DNS, LES) in conjunction with high-order low-dissipation numerical schemes to realistic flow configurations.

One of the most popular choices for specifying these boundaries is the characteristics-based boundary condition^{2–7} where the linearized flow field at the boundaries are decomposed into characteristic waves using either one-dimensional Riemann^{2–5} or other multi-dimensional Riemann approximations.^{6,7} The values of incoming characteristics are then suitably modified. The incoming characteristics are specified at the inflow boundaries, and at the outflow boundaries the variation of the incoming characteristic is zeroed out to ensure no reflection. This, however, makes the problem ill-posed requiring the use of an ad-hoc parameter to allow small reflections that make the solution stable. Generally speaking, such boundary conditions work reasonably well when the characteristic flow direction is normal to the boundary, but reflects spurious energy otherwise.

An alternative to the characteristic-based boundary condition is to add additional “buffer” regions to the main computational domain near the artificial boundaries, and solve a different set of equations in the buffer region in order to minimize acoustic reflections. One approach that has been used involves modeling the pressure fluctuations as acoustic waves propagating in the far-field relative to a single noise-source inside the buffer region.^{8–10} This approach treats vorticity-induced pressure fluctuations the same as acoustic waves. Another popular approach, often referred to as the “sponge layer,” attempts to dampen the flow perturbations by introducing artificial dissipation in the buffer region.¹¹ Although the artificial dissipation removes all perturbations inside the sponge layer, incoming waves are still reflected from the interface boundary between the computational domain and the sponge layer. The effect of these reflections can be somewhat mitigated by appropriately selecting the artificial dissipation strength and the extent of the sponge layer.

One of the most promising variants on the buffer region approach is the Perfectly Matched Layer (PML) technique. The PML technique mitigates spurious reflections from boundaries and interfaces by dampening the perturbation modes inside the buffer region such that their eigenfunctions remain unchanged. The technique was first developed by Berenger¹² for application to problems involving electromagnetic wave propagation. It was later extended to the linearized Euler, Euler and Navier–Stokes equations by Hu and his coauthors.^{13–19} The PML technique ensures the no-reflection property for all waves, irrespective of

*Postdoctoral Fellow, Oak Ridge Associated Universities, Anirban.Garai@nasa.gov

[†]Fundamental Modeling and Simulation Branch, NASA Advanced Supercomputing Division. Scott.M.Murman@nasa.gov

[‡]Fundamental Modeling and Simulation Branch, NASA Advanced Supercomputing Division. Nateri.K.Madavan@nasa.gov

incidence angle, wavelength, and propagation direction. Although the technique requires the solution of a set of auxiliary equations, the computational overhead is easily justified since it allows smaller domain sizes and can provide better accuracy, stability, and convergence of the numerical solution.

In this paper, the PML technique is developed in the context of a high-order spectral-element Discontinuous Galerkin (DG) method. The technique is compared to other approaches to treating the inflow and outflow boundary, such as those based on using characteristic boundary conditions and sponge layers. The superiority of the current PML technique over other approaches is demonstrated for a range of test cases, viz., acoustic pulse propagation, convective vortex, shear layer flow, and low-pressure turbine cascade flow. The paper is structured as follows. We first derive the PML equations from the non-linear Euler equations. A short description of the higher-order DG method used is then described. Preliminary results for the four test cases considered are then presented and discussed. Details regarding current work that will be included in the final paper are also provided.

II. Theory

We first consider the derivation of the x_1 -layer PML equations using the conservative form of the compressible non-linear Euler equation (1):

$$\mathbf{u}_{,t} + \mathbf{F}_i^I{}_{,x_i} = 0, \quad (1)$$

where $\mathbf{u} = \{\rho, \rho u_j, \rho E\}$ is the conservative variable, and \mathbf{F}_i^I is the convective flux; ρ , u_j , $E (= \frac{p}{\gamma-1} + \frac{1}{2}\rho u_j u_j)$, p , and γ are the density, velocity, total energy, pressure, and specific heat ratio, respectively. \mathbf{u} can be partitioned into a mean (a solution of the steady Euler equation, hereafter referred to as the target state), $\bar{\mathbf{u}}$, and a perturbation \mathbf{u}' . It follows from the definition of $\bar{\mathbf{u}}$ that:

$$\overline{\mathbf{F}_i^I}{}_{,x_i} = 0, \quad (2)$$

where $\overline{\mathbf{F}_i^I} = \mathbf{F}_i^I(\bar{\mathbf{u}})$. Note that $\bar{\mathbf{u}}$ does not need to be the exact mean flow, but it should be a close approximation in order to have minimal effect on the final solution.^{17,18} The equations for \mathbf{u}' can then be derived by subtracting equation (2) from equation (1):

$$\mathbf{u}'_{,t} + (\mathbf{F}_i^I - \overline{\mathbf{F}_i^I})_{,x_i} = 0. \quad (3)$$

Performing a Fourier transform on equation (3) we get:

$$(-i\omega)\tilde{\mathbf{u}}' + (\tilde{\mathbf{F}}_i^I - \overline{\tilde{\mathbf{F}}_i^I})_{,x_i} = 0, \quad (4)$$

where $\tilde{\mathbf{u}} = \mathcal{F}(\mathbf{u})$. In order to apply PML layer only in the x_1 direction, the spatial ∂x_1 variable is transformed to $(1 + \frac{i\sigma}{\omega})\partial \check{x}_1$,^{12-14,17} where σ is the absorption coefficient. To ensure that there are no reflections at the interface, σ can vary only in the x_1 direction for the x_1 layer. The PML equation for the perturbed Euler equation thus becomes (the accents on the independent variables are dropped for convenience):

$$(-i\omega)\tilde{\mathbf{u}}' + (\tilde{\mathbf{F}}_i^I - \overline{\tilde{\mathbf{F}}_i^I})_{,x_i} + \sigma\tilde{\mathbf{u}}' + \frac{i\sigma}{\omega}((\tilde{\mathbf{F}}_2^I - \overline{\tilde{\mathbf{F}}_2^I})_{,x_2} + (\tilde{\mathbf{F}}_3^I - \overline{\tilde{\mathbf{F}}_3^I})_{,x_3}) = 0. \quad (5)$$

After defining $\tilde{\mathbf{Q}} = \frac{i}{\omega}((\tilde{\mathbf{F}}_2^I - \overline{\tilde{\mathbf{F}}_2^I})_{,x_2} + (\tilde{\mathbf{F}}_3^I - \overline{\tilde{\mathbf{F}}_3^I})_{,x_3})$, and reverting equation (5) back to the physical coordinate system with equation (2), we can write the PML equations for the x_1 -layer as:

$$\mathbf{u}_{,t} + \mathbf{F}_i^I{}_{,x_i} + \sigma(\mathbf{u} - \bar{\mathbf{u}}) + \sigma\mathbf{Q} = 0, \quad (6a)$$

$$\mathbf{Q}_{,t} = (\mathbf{F}_2^I - \overline{\mathbf{F}}_2^I)_{,x_2} + (\mathbf{F}_3^I - \overline{\mathbf{F}}_3^I)_{,x_3}. \quad (6b)$$

It is important to note that PML equations (6) do not reflect any waves at the interface for electromagnetics,¹² and linear Euler problems¹³ for the continuous equations. However, Hu¹³ noted very small reflections from the interface for the discretized equations.

Hu¹⁴ also showed that the PML equations (6) may become unstable for certain perturbations, even for the linear Euler case with constant mean flow. This instability arises due to the misalignment of the group and phase velocities of the acoustic waves.^{14,16,17} By applying a variable transformation: $\check{t} \rightarrow t + \beta x$,

$\check{x}_i \rightarrow x_i$, where $\beta = \frac{M}{1-M^2}$ the group and phase velocities become perfectly aligned for the linearized Euler case with uniform flow. However, the dispersion relation is hard to determine in the case of more general flows, and Hu¹⁷ reported that $\beta \approx \frac{u_b}{1-u_b^2}$, where u_b is the bulk velocity, is a good approximation. With this given transformation, equations (6) become (the accents on the independent variables are dropped):

$$\mathbf{u}_{,t} + \mathbf{F}_i^I{}_{,x_i} + \sigma(\mathbf{u} - \bar{\mathbf{u}}) + \sigma\beta(\mathbf{F}_1^I - \overline{\mathbf{F}_1^I}) + \sigma\mathbf{Q} = 0, \quad (7a)$$

$$\mathbf{Q}_{,t} = (\mathbf{F}_2^I - \overline{\mathbf{F}_2^I})_{,x_2} + (\mathbf{F}_3^I - \overline{\mathbf{F}_3^I})_{,x_3}. \quad (7b)$$

However, the PML equations (7) may become unstable for large σ with this correction.¹⁷

The PML equations (7) also become unstable in the presence of crossflow,²⁰ since the group and phase velocities become misaligned for vorticity and entropy waves. Using $\check{x}_1 \rightarrow x_1$, $\check{x}_2 \rightarrow x_2 - V_o t$, $\check{x}_3 \rightarrow x_3 - W_o t$, and $\check{t} \rightarrow t$, where V_o and W_o are the bulk velocities in x_2 and x_3 directions respectively, the stability of PML equations (7) improves in the presence of crossflow. Applying this transformation, equations (7) become (the accents on the independent variables are dropped):

$$\mathbf{u}_{,t} + \mathbf{F}_i^I{}_{,x_i} + \sigma(\mathbf{u} - \bar{\mathbf{u}}) + \sigma\beta(\mathbf{F}_1^I - \overline{\mathbf{F}_1^I}) + \sigma\mathbf{Q} = 0, \quad (8a)$$

$$\mathbf{Q}_{,t} + V_o(\mathbf{u} - \bar{\mathbf{u}} + \mathbf{Q})_{,x_2} + W_o(\mathbf{u} - \bar{\mathbf{u}} + \mathbf{Q})_{,x_3} = (\mathbf{F}_2^I - \overline{\mathbf{F}_2^I})_{,x_2} + (\mathbf{F}_3^I - \overline{\mathbf{F}_3^I})_{,x_3}. \quad (8b)$$

Note the final form of PML equations (8) are fully non-linear.

The PML equations for the x_2 and x_3 directions can be derived in a similar fashion. However, one of the initial application areas of this method that is of interest to the authors is DNS of turbomachinery flows where periodic boundary conditions are used in the pitch and span directions. Hence, the PML technique is only implemented and applied in the x_1 or stream-wise direction.

We note that one major issue with regard to implementing any PML approach for subsonic flows is in the specification of the target state. At inflow boundaries, the complete state is known, but at the outflow boundaries the state values are not all known a priori. The complete state needs to be inferred and specified at the outflow boundaries in order to employ the buffer region approach, and the accuracy of the final solution will depend on the quality of this assumption. The approach often used, is to conduct a precursor simulation without any PML, and the solution from this simulation then used as the target state for successive simulations including PML.

Although the PML equations above are (8) are derived from the Euler equations, we use the same form for the Navier–Stokes equations as well. Strictly speaking, one has to solve another set of auxiliary equations in order to apply the PML technique to the Navier–Stokes equations.¹⁸ In general, and in particular for the test cases considered here, the artificial boundaries are typically not located in regions that are dominated by viscosity, and the error from this approximation is likely to be minimal.

III. Numerical method

The spectral-element DG solver used in this paper is described in this section. Using the same form of the PML equations (8) derived for the Euler equations, the Navier–Stokes equations incorporating the x_1 -PML technique can be written as:

$$\mathbf{u}_{,t} + (\mathbf{F}_i^I - \mathbf{F}_i^V)_{,i} + \sigma(\mathbf{u} - \bar{\mathbf{u}}) + \sigma\beta(\mathbf{F}_1^I - \overline{\mathbf{F}_1^I}) + \sigma\mathbf{Q} = 0, \quad (9a)$$

$$\mathbf{Q}_{,t} + V_o(\mathbf{u} - \bar{\mathbf{u}} + \mathbf{Q})_{,x_2} + W_o(\mathbf{u} - \bar{\mathbf{u}} + \mathbf{Q})_{,x_3} = (\mathbf{F}_2^I - \overline{\mathbf{F}_2^I})_{,x_2} + (\mathbf{F}_3^I - \overline{\mathbf{F}_3^I})_{,x_3}. \quad (9b)$$

Next we apply a change of variables $\mathbf{u} = \mathbf{u}(\mathbf{v})$, where \mathbf{v} are the entropy variables

$$\mathbf{v} = \begin{bmatrix} -\frac{s}{\gamma-1} + \frac{\gamma+1}{\gamma-1} - \frac{\rho E}{p} \\ \frac{\rho u_j}{p} \\ -\frac{\rho}{p} \end{bmatrix} \quad (10)$$

with the entropy $s = \log(p/\rho^\gamma)$. The Navier–Stokes equations (9) can be rewritten as:

$$A_0 \mathbf{v}_{,t} + A_i \mathbf{v}_{,x_i} - (K_{ij} \mathbf{v}_{,x_j})_{,x_i} + \sigma(\mathbf{u} - \bar{\mathbf{u}}) + \sigma\beta(\mathbf{F}_1^I - \overline{\mathbf{F}_1^I}) + \sigma\mathbf{Q} = 0, \quad (11a)$$

$$\mathbf{Q}_{,t} + V_o(\mathbf{u} - \bar{\mathbf{u}} + \mathbf{Q})_{,x_2} + W_o(\mathbf{u} - \bar{\mathbf{u}} + \mathbf{Q})_{,x_3} = (\mathbf{F}_2^I - \overline{\mathbf{F}_2^I})_{,x_2} + (\mathbf{F}_3^I - \overline{\mathbf{F}_3^I})_{,x_3}, \quad (11b)$$

with symmetric $A_0 = \mathbf{u}, \mathbf{v}$, $A^i = \mathbf{F}_{i,\mathbf{u}}^I A_0 = \mathbf{F}_{i,\mathbf{v}}^I$ and $K_{ij} = \mathbf{F}_{i,\mathbf{u},x_j}^V A_0 = \mathbf{F}_{i,\mathbf{v},x_j}^V$.²¹

The spatial domain, Ω , is partitioned into non-overlapping hexahedral elements, κ , while the time is partitioned into time intervals (or time-slabs), $I^n = [t^n, t^{n+1}]$. After defining $\mathcal{V}_h = \{\mathbf{w}, \mathbf{w}|_{\kappa} \in [\mathcal{P}(\kappa \times I)]^5\}$, the space-time finite element space is discretized using piece-wise polynomial functions in both space and time. The governing equations (11) are written in weak form as:

$$\begin{aligned} \sum_{\kappa} \left\{ \int_I \int_{\kappa} [-(\mathbf{w}_{,t} \mathbf{u} + \mathbf{w}_{,x_i} (\mathbf{F}_i^I - \mathbf{F}_i^V)) + \mathbf{w}(\sigma(\mathbf{u} - \bar{\mathbf{u}}) + \sigma\beta(\mathbf{F}_1^I - \overline{\mathbf{F}_1^I}) + \sigma\mathbf{Q})] \right. \\ \left. + \int_I \int_{\partial\kappa} \mathbf{w}(\widehat{\mathbf{F}_i^I} \mathbf{n}_i - \widehat{\mathbf{F}_i^V} \mathbf{n}_i) + \int_{\kappa} [\mathbf{w}(t_-^{n+1}) \mathbf{u}(t_-^{n+1}) - \mathbf{w}(t_+^n) \mathbf{u}(t_+^n)] \right\} = 0, \end{aligned} \quad (12a)$$

$$\begin{aligned} \sum_{\kappa} \left\{ \int_I \int_{\kappa} [-(\mathbf{w}_{,t} \mathbf{Q} - \mathbf{w}_{,x_2} (\mathbf{F}_2^I - \overline{\mathbf{F}_2^I}) - \mathbf{w}_{,x_3} (\mathbf{F}_3^I - \overline{\mathbf{F}_3^I})) + \mathbf{w}(V_o(\mathbf{u} - \bar{\mathbf{u}} + \mathbf{Q})_{,x_2} + W_o(\mathbf{u} - \bar{\mathbf{u}} + \mathbf{Q})_{,x_3})] \right. \\ \left. - \int_I \int_{\partial\kappa} \left\{ \mathbf{w}(\widehat{\mathbf{F}_2^I} \mathbf{n}_2 - \overline{\widehat{\mathbf{F}_2^I} \mathbf{n}_2}) + \mathbf{w}(\widehat{\mathbf{F}_3^I} \mathbf{n}_3 - \overline{\widehat{\mathbf{F}_3^I} \mathbf{n}_3}) \right\} + \int_{\kappa} [\mathbf{w}(t_-^{n+1}) \mathbf{Q}(t_-^{n+1}) - \mathbf{w}(t_+^n) \mathbf{Q}(t_+^n)] \right\} = 0, \end{aligned} \quad (12b)$$

where the second and third integrals arise due to the spatial and temporal discontinuity of the basis functions, respectively. $\widehat{\mathbf{F}_i^I} \mathbf{n}_i$ and $\widehat{\mathbf{F}_i^V} \mathbf{n}_i$ denote single-valued numerical flux functions approximating the inviscid and viscous fluxes at the spatial boundaries of the elements, respectively. In this work, the inviscid flux is computed using the Ismail and Roe flux,²² while the viscous flux is computed using the method of Bassi and Rebay.²³ We seek a solution $\mathbf{v} \in \mathcal{V}_h$ that satisfies the weak form equation (12) for all $\mathbf{w} \in \mathcal{V}_h$. The space \mathcal{V}_h is spanned by the tensor product of 1D nodal Lagrange basis functions defined at the Gauss-Legendre points. Integrals in equation (12) are approximated with a quadrature rule using twice the number of quadrature points as solution points in each coordinate direction in order to minimize quadrature errors. The resulting nonlinear system of equations is then solved using a preconditioned Jacobian-free Newton-Krylov solver.^{24, 25}

IV. Results

In order to assess and demonstrate the capabilities of the PML technique, we present solutions for four test-cases: propagation of an acoustic pulse in an inviscid fluid, convection of an isentropic vortex, two-dimensional shear flow, and flow through a low-pressure turbine cascade. In the first test case the flow physics is primarily acoustic, and in the second it is vortical in nature. In the third test case, the shear layer problem, the flow physics is influenced both by vorticity and acoustics. The fourth test-case, the turbine cascade, demonstrates potential of PML in a realistic turbomachinery problem. The results for these test cases using the PML technique are compared to two other techniques currently used to prescribe the boundaries, a characteristic boundary condition without any buffer region, and the sponge layer approach in the x_1 direction. The solutions presented here are all obtained using a spatial 8th-order and temporal 4th-order DG scheme. For remainder of the paper, characteristic boundary simulations will refer to the simulations without any buffer region. For characteristic boundary condition simulations, computational domain consists of domain of interest; whereas for sponge and PML simulations buffer regions were added on either sides of the domain of interest (Figure 1) and the same characteristic boundary conditions were used at the buffer region boundaries (hereafter referred as boundaries).

The sponge layer technique can be simulated using equations (9), by including only $\sigma(\mathbf{u} - \bar{\mathbf{u}})$ in equations (9a), without the need to solve for any equations (9b) for the auxiliary variables \mathbf{Q} . The auxiliary variables \mathbf{Q} were initialized to zero for the PML layer simulations. Boundary conditions (both at the boundary and the interface) for the \mathbf{Q} variable in the x_1 direction for the x_1 -PML layer are not needed (refer to Equations (9b)).

For simulations that incorporate buffer regions, there are two adjustable parameters, the absorption coefficient, σ , and the buffer width. These parameters control the reflections from the interfaces and boundaries for the sponge layer cases, and the reflections from the boundaries for the PML cases. For the PML technique, the stability of the numerical simulation is also a function of σ . One expects that \mathbf{Q} will be zero at a

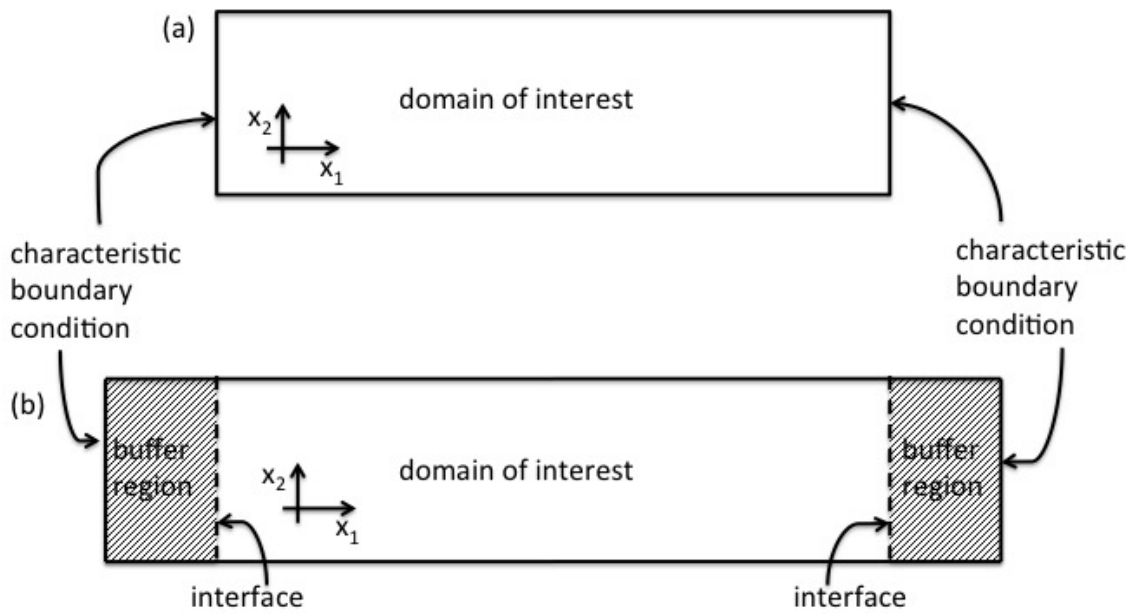


Figure 1. Schematic of computational domains for (a) characteristic boundary condition, and (b) with sponge and PML simulations.

boundary, since the flow solution here should match the target state, and will vary at the interface depending on the incoming disturbances from the domain of interest. Thus, non-zero values for \mathbf{Q} at a boundary indicates the absorption coefficient and/or buffer width for the PML may be too large. The absorption coefficient, σ , was set to zero at the domain of interest region for the sponge layer and PML simulations. Normally σ is increased from a value of zero at the interface to a desired value inside the buffer layer using some power law for finite-difference and finite-volume solvers. However, since discontinuities are handled more efficiently in the DG approach, a constant value for σ is used inside the buffer layer in the present study.¹⁵

A. Acoustic pulse

An acoustic pulse in an inviscid fluid was simulated in the domain, $-3 \leq x_1 \leq 3$, and $-7.5 \leq x_2 \leq 7.5$, using 12 and 30 elements in the x_1 and x_2 directions, respectively. The initial condition was prescribed as: ρ_∞ , $u_{j\infty} = 0$, $p = p_\infty + \frac{p_\infty}{1000} \exp^{-25 \log(2)(x_1^2+x_2^2)}$. Far-field and periodic boundary conditions were used in the x_2 and x_3 directions, respectively. For simulations with buffer regions, two domains of width 1 were added before $x_1 = -3$ and after $x_1 = 3$ using 2 elements in the x_1 direction. The target states at the buffer region were constructed using ρ_∞ , $u_{j\infty}$, and p_∞ . The absorption coefficient was chosen as $\sigma = 1$ for both the sponge layer and PML simulations. The parameters β , V_0 , and W_0 were set to zero as there was no flow in this case for the PML simulations.

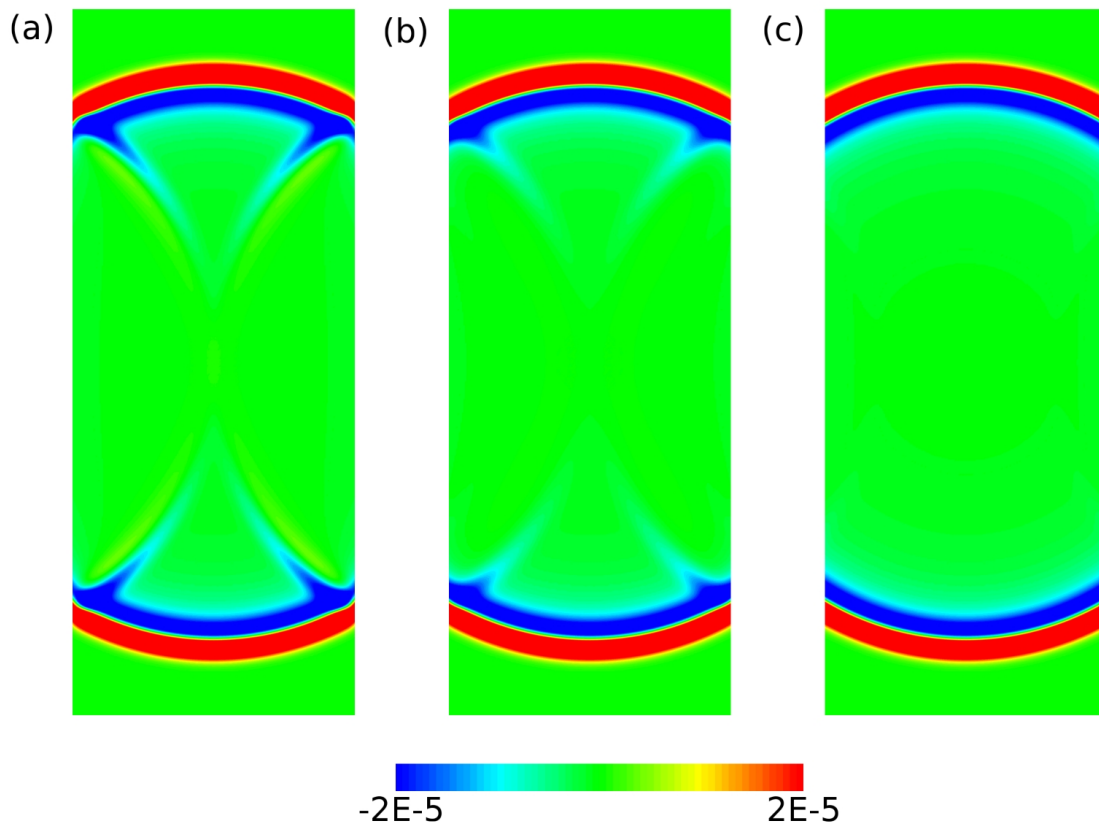


Figure 2. Simulated pressure pulse ($\frac{p_\infty - p}{p_\infty}$) for acoustic pulse simulations with (a) characteristic boundary, (b) sponge layer, and (c) PML. Only the domain of interest, without the buffer regions, is shown in (b – c).

Simulations with the characteristic boundary condition shows strong reflection (Figure 2-a) from the

artificial boundary depending on the incidence angle of the disturbance. The strength of the spurious reflection is low when the incidence disturbance is almost normal to the boundary, and increases with the incidence angle. Reflections from the interface can also be seen with the sponge layer in (Figure 2-b). For the PML simulations, as shown in (Figure 2-c), no spurious reflections are observed.

B. Convective vortex

For the second test case, we consider an isentropic vortex in an inviscid fluid convecting in a $-3 \leq x_1 \leq 3$, and $-7.5 \leq x_2 \leq 7.5$ domain, using 12 and 30 elements in the x_1 and x_2 directions respectively. The initial condition was prescribed as:

$$\delta u_1 = -M_\infty \Gamma \frac{x_2}{R} \exp^{-\frac{x_1^2 + x_2^2}{2}}, \quad (13a)$$

$$\delta u_2 = -M_\infty \Gamma \frac{x_1}{R} \exp^{-\frac{x_1^2 + x_2^2}{2}}, \quad (13b)$$

$$\delta\left(\frac{p}{\rho}\right) = \frac{1}{2} \frac{\gamma}{\gamma - 1} M_\infty^2 \Gamma^2 \exp^{-(x_1^2 + x_2^2)}, \quad (13c)$$

where M_∞ is the convecting speed of the vortex, $\Gamma = \frac{1}{5}$ is the vortex strength, $R = 0.05$ is the characteristic radius. Two different reference states were considered. The first, with flow only in x_1 direction, i.e. ρ_∞ , $u_{1\infty} = M_\infty = 0.1$, $u_{2\infty} = 0$, and p_∞ , will be referred to as Case A; and, the second, with flow in both x_1 and x_2 directions, i.e. ρ_∞ , $u_{1\infty} = u_{2\infty} = M_\infty = 0.5$, and p_∞ , will be referred to as Case B. In Case A, two buffer domains of width 1 were added before $x_1 = -3$ and after $x_1 = 3$ using 2 elements in x_1 direction. In case B, a buffer domain of width 1 (2 elements in the x_1 direction) and another buffer domain of width 2 (4 elements in the x_1 direction) was added before $x_1 = -3$ and after $x_1 = 3$, respectively. Periodic boundary conditions are used in both the x_2 and x_3 directions. The target states at the buffer region were constructed using ρ_∞ , $\mathbf{u}_{j\infty}$, and p_∞ . The absorption coefficient was chosen as $\sigma = 1$ for both the sponge layer and PML simulations. The PML parameter β was calculated as mentioned in the Section II; and $V_0 = 0$ and $W_0 = 0$ were used for the Case A, and $V_0 = 0.5$ and $W_0 = 0$ were used for the Case B simulations. An artificial boundary condition can be considered ideal if the vortex maintains its shape as it approaches and passes through the boundary $x_1 = 3$.

For Case A, the characteristic boundary condition simulation results in strong variations in the shape of the vortex as it passes through the boundary plane (Figures 3-a). Low and high pressure regions develop in the vicinity of the boundary as the vortex propagates through the boundary. Although only marginal improvement in terms of the pressure is noticed for the sponge layer simulation (Figures 3-b), the shape of the momentum contours is substantially improved when compared to the characteristic boundary condition simulation. The results with the PML simulation are clearly superior to both, and no spurious low and high pressure region and no variation in the shape of momentum contour can be discerned (Figures 3-c). However, we note that PML simulations performed with very large values of σ resulted in numerical instabilities even with non-zero β . Similar behavior was observed by Hu.^{14,17}

For case B, the PML simulations were stable only when V_0 was set as bulk velocity in x_2 direction, as observed by Parrish & Hu.²⁰ Inside the PML, all acoustic perturbations are damped exponentially with the exponent taking the form $-\frac{\sigma \cos \phi}{1 + M \cos \phi} x_1$, where M is the characteristic velocity in the x_1 direction and ϕ is the angle between the wave-front normal vector and the x_1 direction.¹⁴ In order to account for this, we have increased the length of the buffer region for the Case B simulation. Small reflections from the interface are noticed for Case B (Figure 4), since the vortex strength is higher in Case B than in Case A. These results are similar to those obtained by Parrish & Hu.²⁰ Results from characteristic boundary condition and sponge layer will be included in the final version of the paper.

C. Shear layer

For the third test case, we consider the inviscid vortex roll-up phenomenon in a 2-D shear layer flow induced by the Kelvin-Helmholtz instability in a computational domain of $-1 \leq x_1 \leq 9$ and $-1 \leq x_2 \leq 1$ with 25

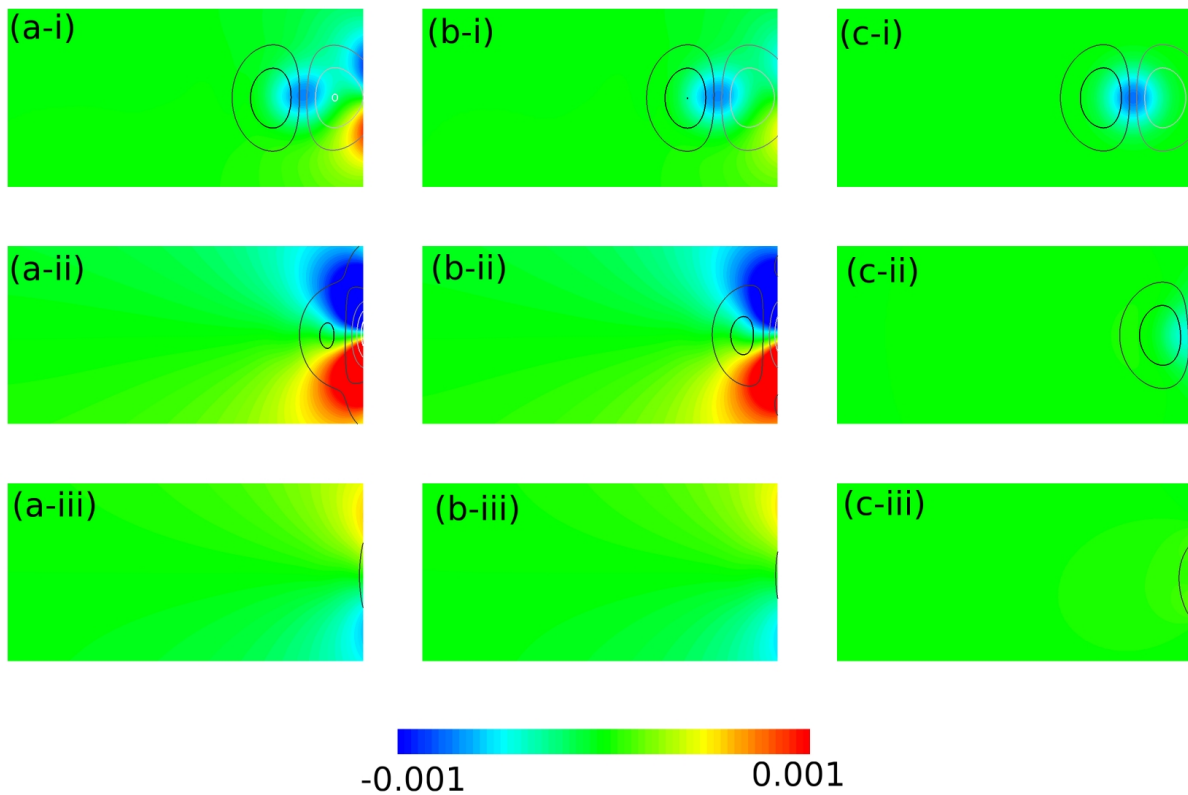


Figure 3. Difference in the pressure ($\frac{p_\infty - p}{p_\infty}$) for a vortex propagating along the x_1 direction from simulations with (a) characteristic boundary, (b) sponge layer, and (c) PML. In (i) the vortex is about to cross the $x_1 = 3$ plane, (ii) half of the vortex has crossed the $x_1 = 3$ plane, and (iii) the entire vortex has crossed the $x_1 = 3$ plane. Black and white contour lines represents the x_2 -momentum. Only the domain of interest is shown in (b - c). The plotted pressure difference can be considered as the error in the pressure for figure (iii).

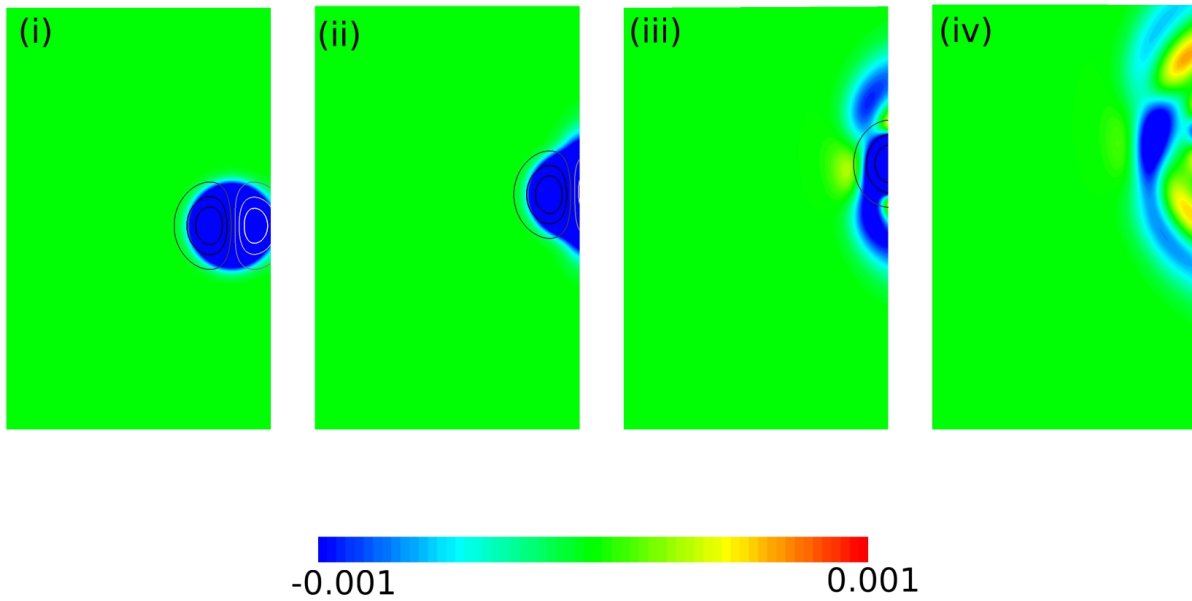


Figure 4. Difference in the pressure ($\frac{p_\infty - p}{p_\infty}$) for vortex propagating along both the x_1 and x_2 directions for simulations using the PML technique. In (i) the vortex is about to cross the $x_1 = 3$ plane, (ii) half of the vortex has crossed the $x_1 = 3$ plane, (iii) the vortex has almost crossed the $x_1 = 3$ plane, and (iv) after the entire vortex has crossed the $x_1 = 3$ plane. Only the domain of interest is shown. The plotted pressure difference can be considered as the error in the pressure for figure (iv).

elements each in the x_1 and x_2 directions. The initial conditions prescribed are given as:

$$\begin{bmatrix} \rho \\ u_1 \\ u_2 \\ p \end{bmatrix} = \begin{bmatrix} \bar{\rho}(x_2) \\ \bar{U}(x_2) \\ 0 \\ \frac{1}{\gamma} \end{bmatrix} \quad (14)$$

where $\bar{U}(x_2) = \frac{1}{2}[(U_1 + U_2) + (U_1 - U_2) \tanh(\frac{2x_2}{\delta})]$, and $\rho(x_2) = \frac{1}{\bar{T}(x_2)}$ with $\bar{T}(x_2) = T_1 \frac{\bar{U}-U_2}{\bar{U}_1-\bar{U}_2} + T_2 \frac{U_1-\bar{U}}{\bar{U}_1-\bar{U}_2} + \frac{\gamma-1}{2}(U_1 - \bar{U})(\bar{U} - U_2)$, with $U_1 = 0.8$, $U_2 = 0.2$, $\delta = 0.4$, $T_1 = 1$, $T_2 = 0.8$. In order to excite the Kelvin–Helmholtz instability, a source function of the form $5 \sin(\frac{\pi}{2}t) \exp^{-\log(2) \frac{(x_1+0.5)^2+(x_2-0)^2}{0.03^2}}$ was used in the energy equation. Far–field and periodic boundary conditions were used in x_2 and x_3 directions, respectively. For simulations with sponge layer and PML, buffer regions of width 0.5 (1 element in x_1 direction) were added at $x_1 \leq -1$ and $x_1 \geq 9$. A value of $\sigma = 10$ was used for both the sponge layer and PML simulations.

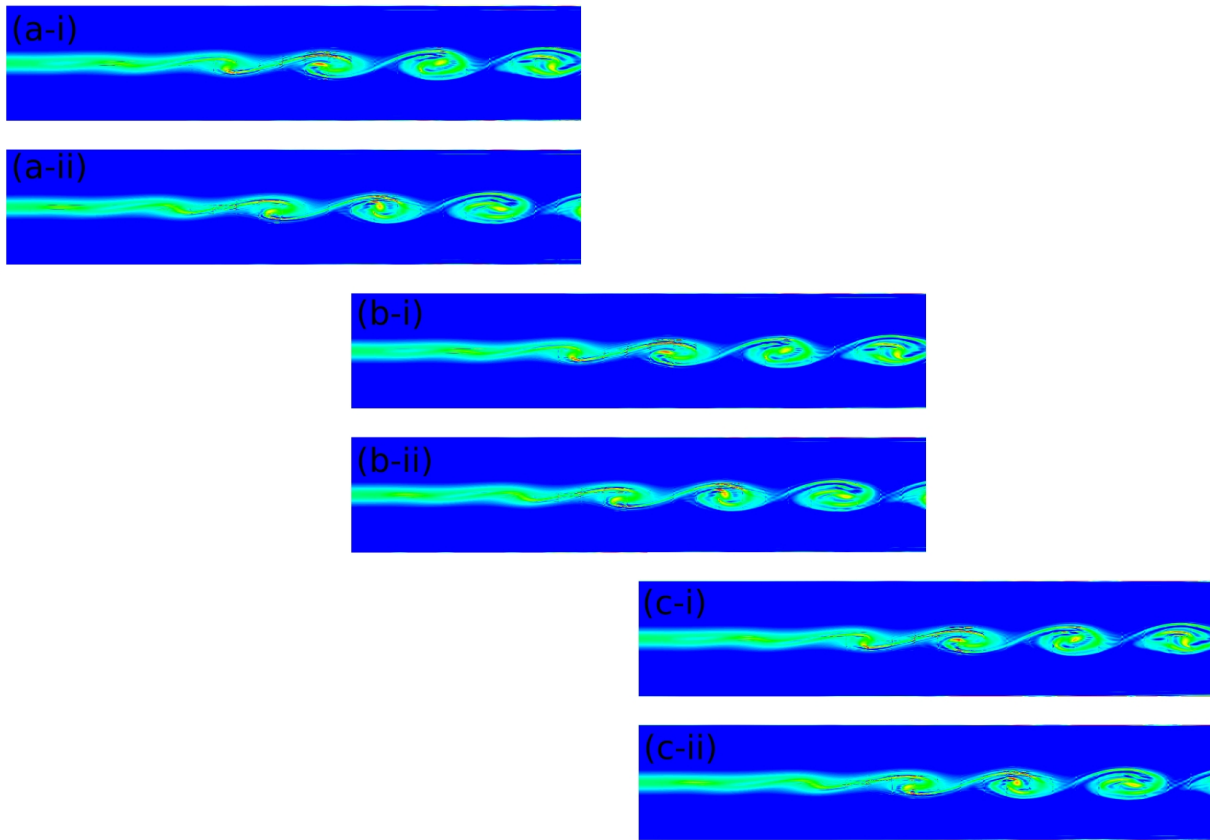


Figure 5. Contours of vorticity magnitude at different time–instants for shear layer simulations with (a) characteristic boundary, (b) sponge layer, and (c) PML.

For these simulations, the target states in the buffer regions were constructed using the initial conditions. Following Hu,¹⁷ a value of $\beta = 1/1.4$ was used, which is close to the value of β when calculated using x_1 bulk velocity. $V_0 = 0$, $W_0 = 0$ were prescribed since there are no cross flow–components for the target state in the buffer regions.

The various boundary conditions, characteristic boundary, sponge layer, and PML, seem to have minimal effect on the variation of vorticity magnitude as the vortex passes through the $x_1 = 9$ plane (Figure 5).

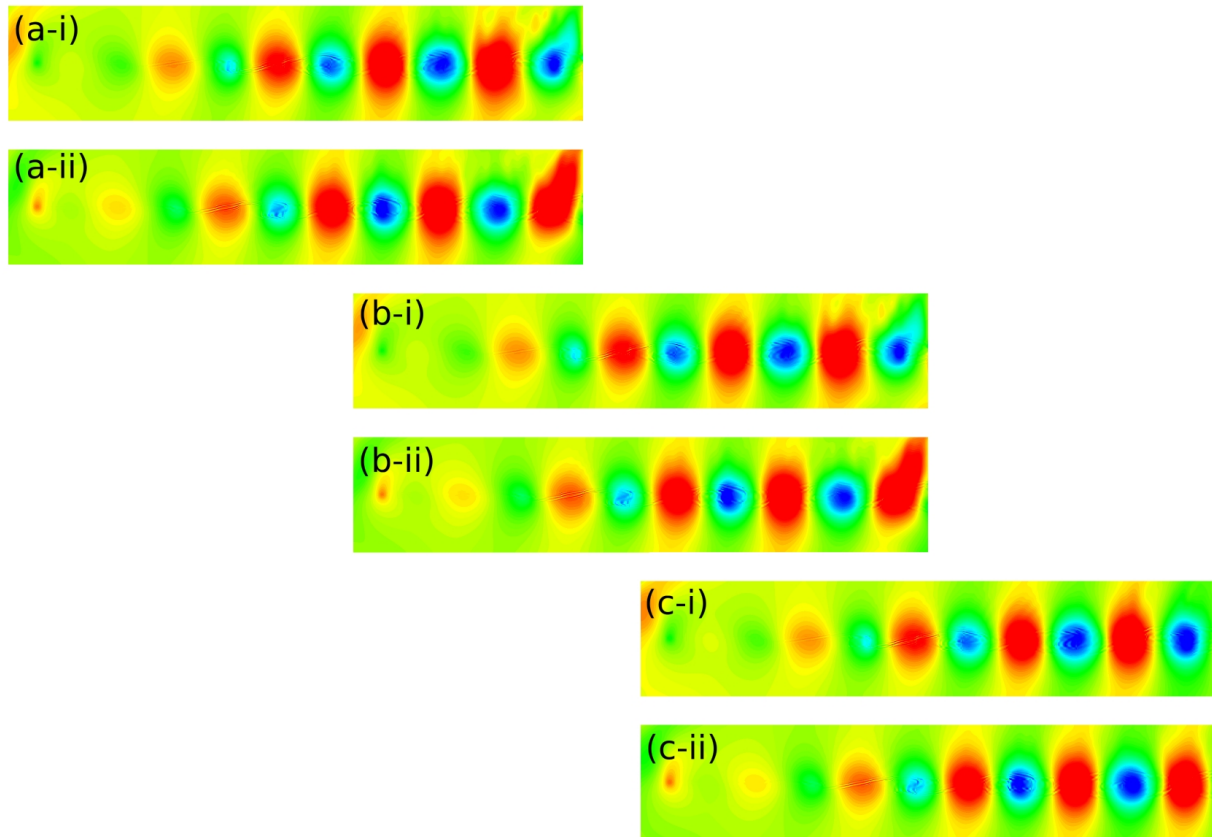


Figure 6. Contours of pressure at different time-instants for shear layer simulations with (a) characteristic boundary, (b) sponge layer, and (c) PML.

However, the effect of the boundary condition is more noticeable in plots of the pressure for the same periods, (Figure 6). With both the characteristic boundary condition and the sponge approach strong spurious reflections are seen, whereas for the PML technique, reflections are hardly noticeable. These spurious reflections also manifest in the value of the mean (time-averaged) pressure. Figure 7 shows the time-averaged pressure for the characteristic boundary condition and PML obtained by averaging over two domain flow-through times. Reflections contaminate the flow and produce low pressure regions near the outflow boundary with the characteristic boundary condition. With the PML technique, the mean pressure varies smoothly except in a localized region very close to the $x_1 = 9$ plane.

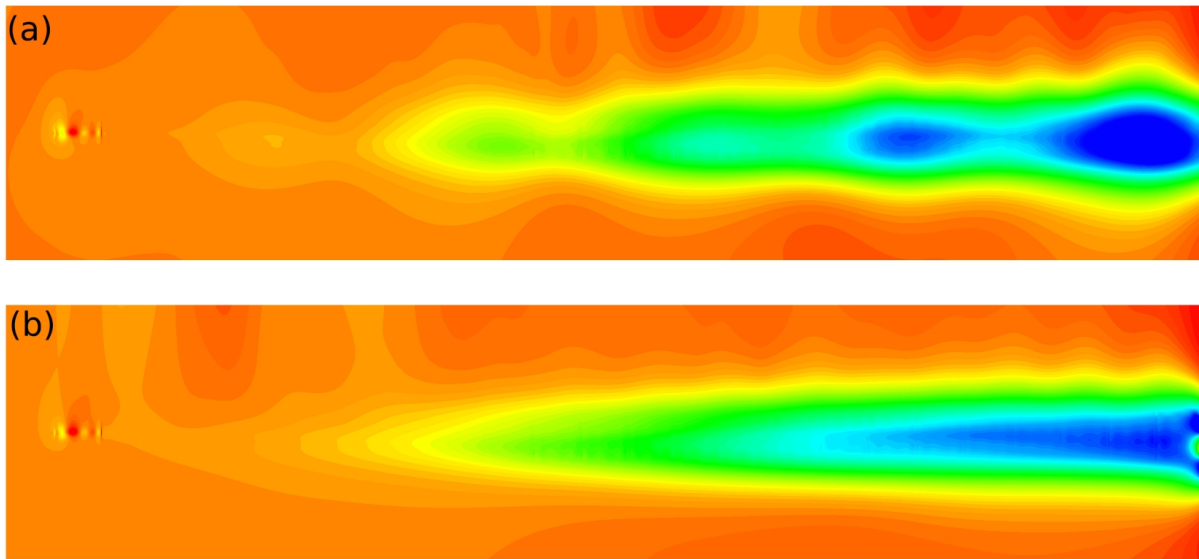


Figure 7. Time-averaged pressure, averaged over two domain flow-through times, for shear layer simulations with (a) characteristic boundary, and (b) PML . Only the domain of interest is shown in (b).

As we have mentioned in Section I, the complete state of the flow at the outflow boundary is often not known in most of practical flows. For these cases, one has to construct a target state at the outflow buffer region. We have tested different approaches of constructing the outflow target state. One approach is to set the target state from the initial condition, but this may not be entirely accurate for the present case, since the shear layer thickens due to vortex roll-up. Another approach is to conduct a precursor simulation (without switching on the outflow buffer region) to gather mean flow statistics, and then use this computed mean flow as a target state for subsequent simulations with the buffer region included. Although the constructed target state may be corrupted due to spurious numerical reflections, this approach will provide mean flow criteria (equation (2)), and will likely be a better choice than any other crude guess, say, based on conserving mass flow rate. We did not notice any difference in numerical results using these two target flow for PML simulations for this test case.

More detailed quantitative results, such as shear layer growth etc, will be presented and compared with analytical results in the final version of the paper.

D. Low-pressure turbine cascade

As a final test case, we apply the PML technique to a practical flow of interest in a realistic configuration, subsonic flow in a low-pressure turbine cascade. We have chosen the well-documented T106A cascade with $Re = 60000$, based on isentropic exit speed and chord length, and in the absence of any inflow turbulence. Details of the problem set-up can be found at Garai et al.²⁶ Buffer regions extending about one quarter axial-chord length (with two elements in x_1 direction) were added at the inflow and outflow boundary. The absorption coefficient, σ , was chosen as 10. At the inflow buffer region, the target state was set to the inflow condition. As full state at the outflow was not known from experimental data, a precursor simulation spanning 4 domain flow-through times was first performed, and mean flow statistics were gathered for the last 2 domain flow-through times. This calculated mean flow was then used as the target state for the outflow buffer region for the simulations using the sponge layer and PML technique. Periodic boundary conditions were used in the pitch-wise and span-wise directions. PML parameters, β , V_0 and W_0 were calculated using inflow conditions for the inflow PML, and using the calculated mean from the precursor simulations for the outflow PML.

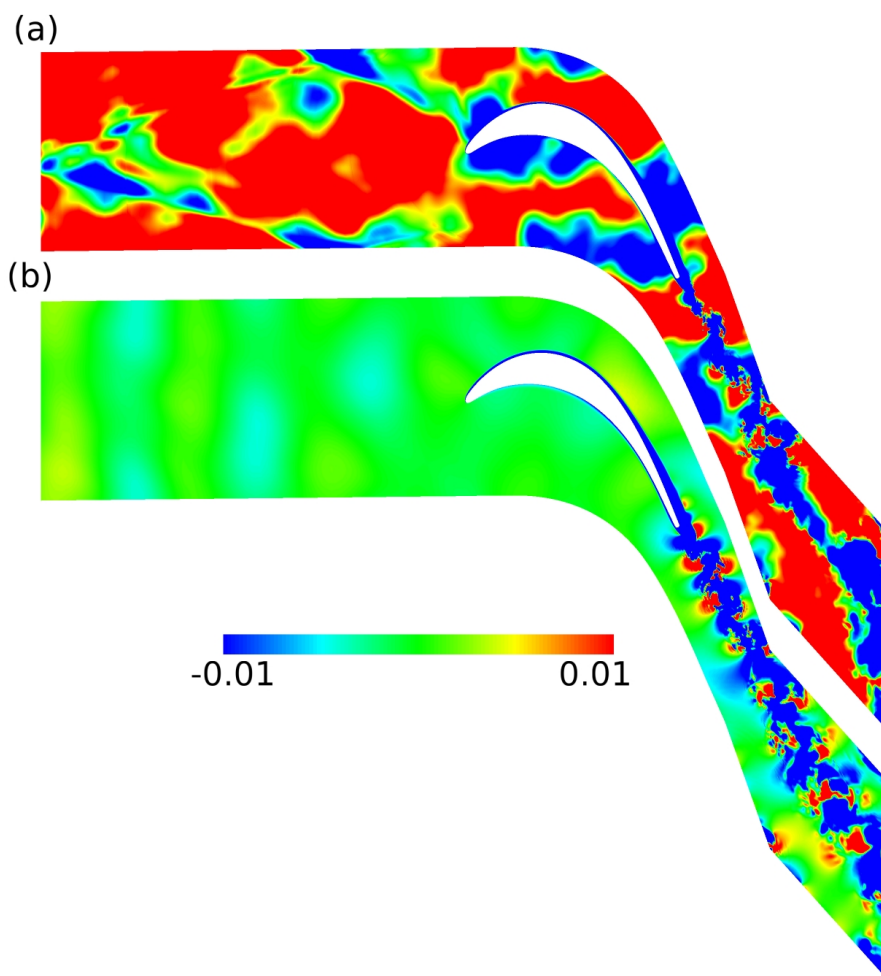


Figure 8. Contours of total pressure difference ($\frac{P_{t,inflow} - P_t}{P_{t,inflow}}$) for the low-pressure turbine cascade simulation with (a) characteristic boundary, and (b) PML.

Variation of the total pressure with respect to the inflow total pressure is plotted for both the characteristic

boundary condition, and the PML in Figure 8. (Sponge layer simulation is currently ongoing, and will be presented in the final version of the paper). Spurious reflection from non-normal disturbances incident on the inflow plane is clearly evident in the simulation with characteristic boundary condition (Figure 8–a). These spurious reflections die down very slowly as they reflect back and forth between inflow and airfoil. Thus they tend to increase the total pressure with respect to the inflow condition, and affect the vortex shedding process at the stationary state. On the other hand the PML damps the numerical acoustic disturbances without any spurious reflection (Figure 8–b), and the total pressure equilibrates with the inflow condition at the stationary state.

V. Plan for Final Paper

The PML technique developed here for a spectral-element DG method shows promise in accurately representing the inflow and outflow boundaries in truncated computational domains. It is shown to be superior to techniques based on characteristics boundary conditions, or the use of sponge layers for the test cases considered here. The results for the turbine cascade are particularly encouraging, since the lack of proper non-reflecting inflow and outflow boundaries is a major issue in internal flows such as turbomachinery where spurious acoustic reflections can often swamp the solution and lead to poor (or non) convergence and inaccurate results.

In the final version of the paper, we plan to provide more quantitative comparisons between the PML and other techniques. We will also address and quantify the impact of errors due to using the discretized PML that can only be mitigated by proper choice of the absorption coefficient, σ and the thickness (width) of the PML. We will also address the issue of the PML equations tending to become unstable for large value of σ and will examine the limiting value of σ from the entropy stability perspective.

Acknowledgments

Funding for Anirban Garai was provided by the Advanced Air Transport Technology Project in the NASA Advanced Air Vehicles Program through the NASA Postdoctoral Program administrated by Oak Ridge Associated Universities (ORAU). The authors thank Laslo T. Diosady, NASA Ames Research Center, for providing the spectral-element DG code and for many helpful discussions.

References

- ¹Colonius, T., “Modeling Artificial Boundary Conditions for Compressible Flow,” *Annual Review of Fluid Mechanics*, Vol. 36, 2004, pp. 315–345.
- ²Hedstrom, G. W., “Nonreflecting Boundary Conditions for Nonlinear Hyperbolic Systems,” *Journal of Computational Physics*, Vol. 30, 1979, pp. 222–237.
- ³Thompson, K. W., “Time Dependent Boundary Conditions for Hyperbolic Systems,” *Journal of Computational Physics*, Vol. 68, 1987, pp. 1–24.
- ⁴Giles, M. B., “Nonreflecting Boundary Conditions for Euler Equation Calculations,” *AIAA Journal*, Vol. 28, No. 12, 2015/05/15 1990, pp. 2050–2058.
- ⁵Poinsot, T. J. and Lele, S. K., “Boundary Conditions for Direct Simulations of Compressible Viscous Flows,” *Journal of Computational Physics*, Vol. 101, 1992, pp. 104–129.
- ⁶Lappas, T., Leonard, A., and Dimotakis, P. E., “Riemann Invariant Manifolds For the Multidimensional Euler Equations,” *SIAM Journal of Scientific Computing*, Vol. 20, No. 4, 1999, pp. 1481–1512.
- ⁷Liu, Q. and Vasilyev, O. V., “Nonreflecting Boundary Conditions Based on Nonlinear Multidimensional Characteristics,” *International Journal for Numerical Methods in Fluids*, Vol. 62, 2010, pp. 24–55.
- ⁸Tam, C. K. W. and Webb, J. C., “Dispersion-Relation-Preserving Finite-Difference Schemes for Computational Acoustics,” *Journal of Computational Physics*, Vol. 107, 1993, pp. 262–281.
- ⁹Tam, C. K. W. and Dong, Z., “Radiation and Outflow Boundary Conditions for Direct Computation of Acoustic and Flow Disturbances in Nonuniform Mean Flow,” *Journal of Computational Acoustics*, Vol. 4, 1996, pp. 175–201.
- ¹⁰Bogey, C. and Bailly, C., “Three-Dimensional Non-Reflective Boundary Conditions for Acoustic Simulations: Far Field Formulation and Validation Test Cases,” *Acta Acoustics*, Vol. 88, 2002, pp. 463–471.
- ¹¹Israeli, M. and Orszag, S. A., “Approximation of Radiation Boundary Conditions,” *Journal of Computational Physics*, Vol. 41, 1981, pp. 115–135.
- ¹²Berenger, J.-P., “A Perfectly Matched Layer for the Absorption of Electromagnetic Waves,” *Journal of Computational Physics*, Vol. 114, No. 2, 1994, pp. 185 – 200.
- ¹³Hu, F. Q., “On Absorbing Boundary Conditions for Linearized Euler Equations by a Perfectly Matched Layer,” *Journal of Computational Physics*, Vol. 129, No. 1, 1996, pp. 201 – 219.

- ¹⁴Hu, F. Q., “A Stable, Perfectly Matched Layer for Linearized Euler Equations in Unsplit Physical Variables,” *Journal of Computational Physics*, Vol. 173, No. 2, 2001, pp. 455 – 480.
- ¹⁵Hu, F. Q. and Atkins, H. L., “A Discrete Analysis of Non-reflecting Boundary Conditions for Discontinuous Galerkin Method,” *AIAA Paper*, 2003.
- ¹⁶Hu, F. Q., “A Perfectly Matched Layer Absorbing Boundary Condition for Linearized Euler Equations with a Non-Uniform Mean Flow,” *Journal of Computational Physics*, Vol. 208, No. 2, 2005, pp. 469 – 492.
- ¹⁷Hu, F. Q., “Development of PML Absorbing Boundary Conditions for Computational Aeroacoustics: A Progress Review,” *Computers Fluids*, Vol. 37, No. 4, 2008, pp. 336 – 348.
- ¹⁸Hu, F. Q., Li, X., and Lin, D., “Absorbing Boundary Conditions for Nonlinear Euler and Navier–Stokes Equations Based on the Perfectly Matched Layer Technique,” *Journal of Computational Physics*, Vol. 227, No. 9, 2008, pp. 4398 – 4424.
- ¹⁹Lin, D., Li, X., and Hu, F. Q., “Absorbing Boundary Condition for Nonlinear Euler Equations in Primitive Variables Based on the Perfectly Matched Layer Technique,” *Computers Fluids*, Vol. 40, No. 1, 2011, pp. 333 – 337.
- ²⁰Parrish, S. A. and Hu, F. Q., “PML Absorbing Boundary Conditions for the Linearized and Nonlinear Euler Equations in the Case of Oblique Mean Flow,” *International Journal for Numerical Methods in Fluids*, Vol. 60, No. 5, 2009, pp. 565–589.
- ²¹Hughes, T. J. R., Franca, L., and Mallet, M., “A New Finite Element Formulation for Computational Fluid Dynamics I: Symmetric Forms of the Compressible Euler and Navier–Stokes Equations and the Second Law of Thermodynamics,” *Computer Methods in Applied Mechanics and Engineering*, Vol. 54, 1986, pp. 223–234.
- ²²Ismail, F. and Roe, P. L., “Affordable, Entropy-Consistent Euler Flux Functions II: Entropy Production at Shocks,” *Journal of Computational Physics*, Vol. 228, 2009, pp. 5410–5436.
- ²³Bassi, F. and Rebay, S., “GMRES Discontinuous Galerkin Solution of the Compressible Navier–Stokes Equations,” *Discontinuous Galerkin Methods: Theory, Computation and Application*, Springer, Berlin, 2000, pp. 197–208.
- ²⁴Diosady, L. T. and Murman, S. M., “Higher–Order Methods for Compressible Turbulent Flows Using Entropy Variables,” *AIAA Paper 2015-0294*, 2015.
- ²⁵Diosady, L. T. and Murman, S. M., “DNS of Flows over Periodic Hills Using a Discontinuous-Galerkin Spectral-Element Method,” *AIAA Paper 2014-2784*, 2014.
- ²⁶Garai, A., Diosady, L. T., Murman, S. M., and Madavan, N. K., “DNS of Flow in a Low–Pressure Turbine Cascade Using a Discontinuous–Galerkin Spectral–Element Method,” *ASME Turbo Expo Paper GT2015-42773*, 2015.